PAPER

Synchronization and bundling of anchored bacterial flagella†

Shang Yik Reigh,* Roland G. Winkler* and Gerhard Gompper*

The synchronization and bundling process of bacterial flagella is investigated by mesoscale hydrodynamic simulations. Systems with two to six flagella are considered, which are anchored at one end, and are driven by a constant torque. A flagellum is modelled as a linear helical structure composed of mass points with their elastic shape maintained by bonds, bending, and torsional potentials. The characteristic times for synchronization and bundling are analyzed in terms of motor torque, separation, and number of flagella. We find that hydrodynamic interactions determine the bundling behavior. The synchronization time is smaller than the bundling time, but their ratio depends strongly on the initial separation. The bundling time decreases with increasing number of flagella at a fixed radius in a circular arrangement due to multi-helix hydrodynamics.

1 Introduction

Peritrichous bacteria, such as *E. coli*, are covered by multiple flagella, which are essential for their locomotion. An individual flagellum is of helical shape and driven by a rotary motor that is attached to the bacteria's cell body.[1,2] When all the left- (right-) handed flagella turn counterclockwise (clockwise), they form a single helical bundle and the bacterium moves forward.[3–10] Fundamental to the concerted motion of the bundle is the synchronized and in-phase rotation of the various flagella.[11,12]

The bacteria's steady forward motion, denoted as "running" phase, is interrupted by short periods of "tumbling". [13–15] The alternate running and tumbling allows the bacteria to change the direction of motion and to perform a biased random walk by adjusting the duration of the running phase to the environmental conditions. This enhances the search efficiency for favorable locations like highly concentrated regions of chemical compounds (chemotaxis).[2,16] Tumbling is initiated by rotation of one of the flagella in the opposite direction.[17,18] Then, this flagellum leaves the bundle and the bacterium changes the swimming direction. When the reversely rotating motor changes its rotation back to its initial direction, the separated flagellum joins the bundle again.[5,15] During bundling, tumbling, and re-bundling, the helical pitch and the radius of a flagellum changes; it undergoes "polymorphic transformations".[19–27]

Locomotion of bacteria has been studied for many years.[1–26,28–34] Experimentally, dark-field microscopy[28] and

Theoretical Soft Matter and Biophysics, Institute of Complex Systems and Institute for Advanced Simulation, Forschungszentrum Jülich, 52425 Jülich, Germany. E-mail: s.y.reigh@fz-juelich.de; r.winkler@fz-juelich.de; g.gompper@fz-juelich.de

† Electronic supplementary information (ESI) available: Three movies showing simulation animations of synchronization and bundling of several helical flagella. See DOI: 10.1039/c2sm07378a

fluorescence microscopy provide insight into the swimming behavior of bacteria.[13,14] Specifically, bundle formation has been studied by macroscopic experiments.[3,4] By using helical metal wires it has been shown that the wrapping of flagella occurs in a right-handed sense for left-handed flagella with an in-phase relationship between flagella.[3] Experiments of the bundling process using polymer tubes in viscous fluids support the observation that the left-handed helices are twisted around each other in a right-handed manner without jamming.[4]

Numerical investigations using Stokes equations for fluids and various models for a flagellum, such as bead-spring models, provide insight into the bundling process and the run-and-tumble dynamics.[5,10,15,35] The propulsion dynamics, the flow field, and the polymorphic transitions of a flagellum have been investigated by an elastic network model in ref. 10. The flow fields have been studied in ref. 5 of three flagellum during the run as well as the tumbling phase. The linear dependence of the swimming velocity and the flagellum rotation frequency was verified. Moreover, the simulations confirm that hydrodynamic interactions can lead to bundle formation, and that the fluid flow generated by the rotation of the flagella draws them together and enhances the bundling process.[5] By simulations exploiting the Rotne–Prager–Yamakawa hydrodynamic tensor, the run-and-tumble motion of a bacterium has been studied and the fluid flow patterns have been discussed.[15] The simulations suggest that the bacterium-induced flow magnitude is large enough to affect the transport of surrounding chemo-attractants. By a similar approach, the bundling process of two flagella have been studied.[35] Here, multiple coexisting bundling states are found, with either tight bundles, where the flagella are in mechanical contact, or loose bundles, with flagella intertwined but not touching, depending on the initial state.

Aside from the considerations in ref. 35, little is known about the synchronization of flagella rotation, phase stability during

rotation, or bundle stability. These aspects will depend on the number of flagella included in a bundle and their spatial arrangement. Moreover, the role of hydrodynamic interactions in these processes has not been investigated. The stability and efficiency of the bundling process is vital for bacteria and deserves special attention.

In this article, we discuss bundle formation for systems of various flagella by using mesoscale hydrodynamic simulations exploiting the multiparticle collision dynamics (MPC) approach.[36,37] This method has been shown to correctly account for hydrodynamic interactions and therefore allows us to study the influence of such interactions in bundle formation. In section 2, we will outline the model for the solvent and the helical filament. Section 3 presents results for various numbers of helices, starting from two up to six helices. Finally, section 4 summarizes our findings.

2 Simulation method, model

In order to simulate mesoscopic systems, a hybrid simulation approach has been suggested, combining molecular dynamic simulations (MD) for embedded (elastic) particles with the MPC method for the fluid.[36,37] The approach has successfully been applied to the hydrodynamic behavior of many soft matter systems, such as colloidal suspensions,[38–45] polymer solutions,[46–52] vesicles and blood cells,[53,54] as well as the swimming behavior of sperm cells[55,56] and diffusiophoretic swimmers.[57]

2.1 Fluid model

MPC is a particle-based simulation approach, where the fluid is represented by N_s point particles of mass m with positions $\boldsymbol{r}_i(t)$ and velocities $\boldsymbol{v}_i(t)$, where $i = 1,...,N_s$. The algorithm consists of alternating streaming and collision steps. In the streaming step, the particles move ballistically and their positions change according to

$$\boldsymbol{r}_i(t + h) = \boldsymbol{r}_i(t) + h\boldsymbol{v}_i(t) \qquad (1)$$

in the time interval h, which denotes the collision time. In the collision step, the particles are sorted into cubic cells of side length a and their relative velocities, with respect to the center-of-mass velocities of each cell, are rotated around a randomly oriented axis by a fixed angle α. Thus, the particle velocity after collision is given by

$$\boldsymbol{v}_i(t + h) = \boldsymbol{v}_{cm}(t) + \mathscr{R}(\alpha)(\boldsymbol{v}_i(t) - \boldsymbol{v}_{cm}(t)), \qquad (2)$$

where $\mathscr{R}(\alpha)$ is the rotation matrix and $\boldsymbol{v}_{cm} = \Sigma_{j=1}^{N_c}\boldsymbol{v}_j/N_c$ is the center-of-mass velocity of the particles in the cell to which the particle i belongs, and N_c is the number of particles in that cell.[36,37,58,59] A random shift of the collision lattice is applied at every collision step to ensure Galilean invariance.[60] A constant temperature is maintained locally by velocity scaling at every collision cell and every collision step.[59]

2.2 Flagellum model

We consider a bacterial flagellum as a coarse-grained macro-molecular system embedded in an MPC fluid and represent it as helical sequence of N_m points of mass M_h. These points interact
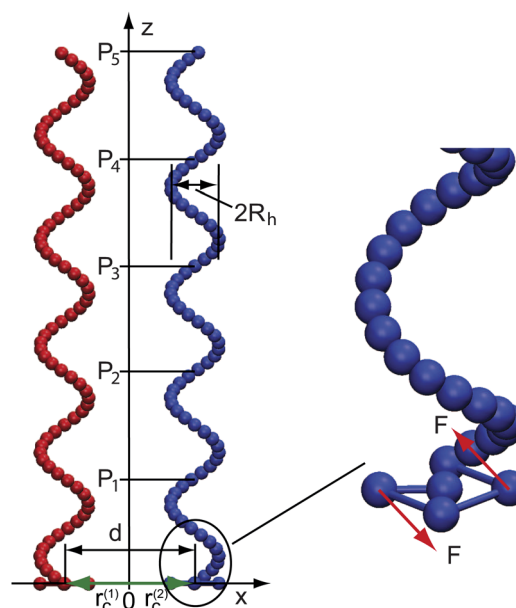
Fig. 1 Model of flagella. The base part consists of five beads. The central bead is trapped in a three-dimensional harmonic potential. The four peripheral beads are trapped in a one-dimensional harmonic potential along the z-axis. The external force is symmetrically applied on two beads.

with each other by bonds, bond bending, and torsional potentials.[61] A repulsive and truncated Lennard–Jones potential is used to account for excluded-volume interactions, which prevent flagella from crossing each other. Explicitly, the potentials are given by

- bond potential

$$U_{\text{bond}} = \frac{\kappa_{\text{bond}}}{2} \sum_{i=2}^{N_m} \left(|\boldsymbol{R}_i - \boldsymbol{R}_{i-1}| - l_0 \right)^2, \qquad (3)$$

- bond bending potential

$$U_{\text{bend}} = \frac{\kappa_{\text{bend}}}{2} \sum_{i=3}^{N_m} \left(\cos\theta_i - \cos\theta_0 \right)^2, \qquad (4)$$

- torsional potential

$$U_{\text{tors}} = \frac{\kappa_{\text{tors}}}{2} \sum_{i=4}^{N_m} \left(\cos\varphi_i - \cos\varphi_0 \right)^2, \qquad (5)$$

- repulsive Lennard–Jones potential

$$U_{LJ} = \begin{cases} 4\varepsilon \left[\left(\dfrac{\sigma}{R} \right)^{12} - \left(\dfrac{\sigma}{R} \right)^{6} \right] + \varepsilon, & R < 2^{1/6}\sigma, \\ 0, & \text{otherwise,} \end{cases} \qquad (6)$$

where $\boldsymbol{R}_i$ is the position vector of bead i, R is the distance between non-bonded particles, l_0, θ_0, and φ_0 are the equilibrium bond length, bending angle, and torsional angle, respectively. κ_{bond}, κ_{bend}, and κ_{tors} are the bond, bending, and torsional force constants, respectively. The bending angle follows from the relation $\cos\theta_i = (\Delta\boldsymbol{R}_i \cdot \Delta\boldsymbol{R}_{i-1})/(|\Delta\boldsymbol{R}_i||\Delta\boldsymbol{R}_{i-1}|)$, and the torsional angle from $\cos\varphi_i = (\Delta\boldsymbol{R}_i \times \Delta\boldsymbol{R}_{i-1})(\Delta\boldsymbol{R}_{i-1} \times \Delta\boldsymbol{R}_{i-2})/(|\Delta\boldsymbol{R}_i \times \Delta\boldsymbol{R}_{i-1}||\Delta\boldsymbol{R}_{i-1} \times \Delta\boldsymbol{R}_{i-2}|)$, where $\Delta\boldsymbol{R}_i = \boldsymbol{R}_i - \boldsymbol{R}_{i-1}$.[61]

Additionally, five beads are added in a plane at the base of the helix (see Fig. 1). One bead is located at the center of the helix and the other four are arranged on a square around the central bead. These five beads define the plane from which the helix orientation and pitch are measured. The beads interact with each other by bonds, bond bending, and torsional potentials similar to those of the helix. The five beads are trapped in constraining potentials. The central bead is confined in a three dimensional harmonic potential, i.e., it is fixed in space, whereas the peripheral beads are restrained along the z-axis by a one-dimensional harmonic potential. The potentials are of the form

$$U_r = \frac{\kappa_{cf}}{2}(\mathbf{r} - \mathbf{r}_c)^2,\qquad(7)$$

where $\mathbf{r}_c$ is either the equilibrium position of the central particle or the z-coordinate of the peripheral beads; in the latter case, the x- and y-coordinates are unconstrained. Hence, the flagellum is not allowed to perform any translational motion but rotates around a central bead driven by an external torque. In the stationary state, the helices are force-free along the z-direction and the fluid moves with a constant average velocity in the positive z-direction. This corresponds to a free swimmer, moving with a constant velocity in a resting fluid.

The dynamics of the mass points is described by Newton's equations of motion, which are integrated by the velocity–Verlet algorithm with time step h_p.[61] The flagellum is set up as a left-handed helix. Symmetrical forces are applied in a counterclockwise direction when watched from the distal end, which generates a torque $M = 2R_hF$ pointing into the positive z-direction, where R_h is the helix radius and F the applied force, without any external net force.

The bead particles are coupled to the fluid in the collision step. Similar to the fluid particles, the relative velocities of beads in a particular collision cell are rotated. Hence, the velocity of a bead after a collision is given by eqn (2), with the modified center-of-mass velocity of a cell with N_M beads

$$\mathbf{v}_{cm} = \frac{m\sum_{i=1}^{N_c}\mathbf{v}_i + M_h\sum_{i=1}^{N_M}V_i}{mN_c + M_hN_M},\qquad(8)$$

where V_i is the velocity of bead i. This results in an exchange of momentum between the beads and fluid particles whilst conserving momentum.[37,46]

2.3 Parameters

The size of the simulation box is taken to be $L_x \times L_y \times L_z = (70 \times 70 \times 80\,a^3)$, $(120 \times 120 \times 80\,a^3)$, or $(100^3\,a^3)$, where a is the side length of the collision cell, depending on the distances between the helices. The transport properties of the solvent depend on h, α, and N_c.[36,37,52] Tuning these parameters allows us to attain solvents with a high Schmidt number and a low Reynolds number Re. The choice $N_c = 10$, $\alpha = 130°$, and $h/\sqrt{ma^2/(k_BT)} = 0.1$, where T is the temperature and k_B is the Boltzmann constant, yields the solvent viscosity $\eta = mN_c\nu = 8.7\sqrt{mk_BT/a^4}$, where ν is the kinematic viscosity, and the Schmidt number $Sc = 17$, which ensures that momentum transport dominates over mass transport.[38] In order to confirm low-Reynolds-number behavior, we additionally consider the

collision time steps $h/\sqrt{ma^2/(k_BT)} = 0.05$, 0.02, and 0.01, where η scales linearly with $1/h$.

Only left-handed flagella are considered. The mass of a flagellum bead is set to $M_h = 10m$. The number of beads for a five-turn helix is $N_m = 78$, with the equilibrium bond length $l_0 = a = \sigma$, the bending angle $\theta_0 = 20°$, and the equilibrium torsional angle $\varphi_0 = 166°$, which yields, with the radius of a flagellum $R_h = 2a$, the helix pitch $P \approx 8.8a$ and helix angle $\psi = 55°$. Thus, the pitch is close to that of E. coli in the semi-coiled state and somewhat smaller than the pitch of the normal state.[20] The bond, bond bending, and torsional force constants are $\kappa_{bond}/(k_BT/l_0^2) = 10^5$, $\kappa_{bend}/(k_BT) = 2 \times 10^5$, and $\kappa_{tors}/(k_BT) = 10^5$, respectively. The temperature is $k_BT/\varepsilon = 1$. The distribution of the bond, bending, and torsional energies follow the corresponding Maxwell–Boltzmann distributions. The constraining-force constant of the motor part is $\kappa_{cf}/(k_BT/l_0^2) = 10^4$. During the simulations up to $t/\sqrt{ma^2/(k_BT)} = 6000$, corresponding to 3×10^6 MD time steps of length $h_p/\sqrt{ma^2/(k_BT)} = 0.002$, synchronization and bundling are completed.
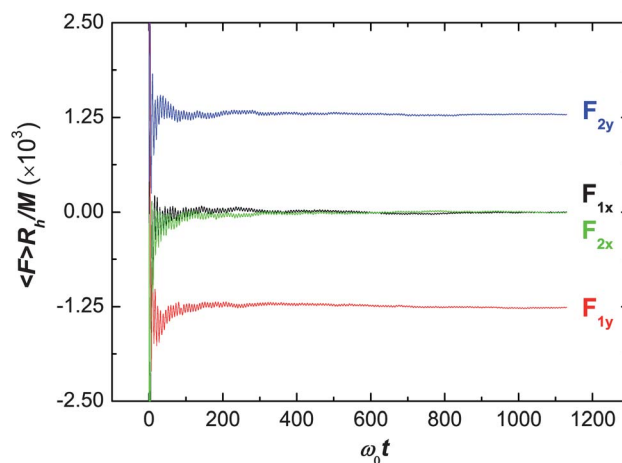

Fig. 2 Average forces along the x- and y-direction (F_{ix}, F_{iy}) on two rotating helices (1,2) with constraining axial potentials for the separation $d/R_h = 2.5$.
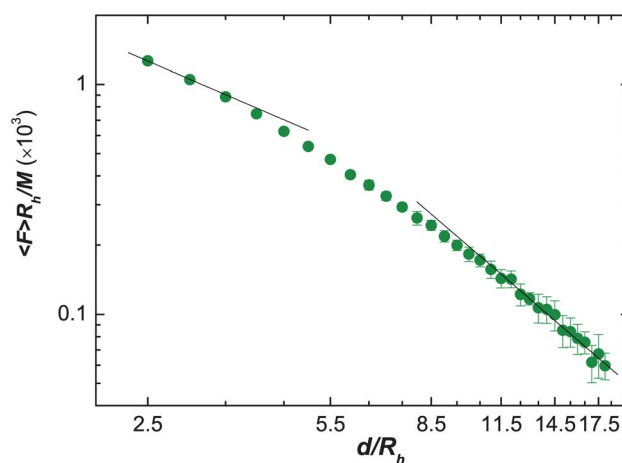

Fig. 3 Magnitude of the tangential forces as a function of distance d for a system of two aligned helices. Lines indicate the power laws d^{-1} and d^{-2} for the limiting cases of small and large helix separations, respectively.

3 Results

Synchronization of the rotational motion between different flagella is a prerequisite for the formation of tight bundles. We will present results for the synchronization and bundling process as function of time, helix separation, and applied torque.

3.1 Two helices

The bundling behavior of systems of two helices has been studied in ref. 35 with an Oseen-tensor based hydrodynamic approach. Our systems behave very similarly, therefore we do not discuss this case in detail. Similarities and differences will be stressed in the discussion of the behavior of several helices. Here we briefly address the hydrodynamics of two helices, which provides a hint of a possible mechanism for bundle formation.

For this purpose, we consider two helices with their center-lines separated by a distance d. A snapshot of a single helix is displayed in Fig. 1. In order to investigate the forces governing bundle formation, we constrain the orientation of both helices such that they are nearly parallel. This is achieved by confining every bead in a harmonic potential along a circle with the radius of the helix R_h

$$U_{ax} = \frac{\kappa_{ax}}{2} \sum_{i=1}^{N_m} (|\mathbf{R}_i - \mathbf{R}_{ch}| - R_h)^2 . \tag{9}$$

$\mathbf{R}_{ch}$ has the same x and y component as the central particle of the base $\mathbf{r}_c$ and the same z component as $\mathbf{R}_i$ initially. For the force constant κ_{ax} the same value is used as for κ_{cf}.

Counterclockwise rotation of each helix is achieved by the same constant torque $M/k_B T = 800$. Average forces

$$\langle \mathbf{F} \rangle = \frac{1}{t} \int_0^t \mathbf{F}(t') dt' \tag{10}$$

along the x- and y-axis, calculated from the potential (9), are shown in Fig. 2 as function of $\omega_0 t$, where $\omega_0 = 0.113 \sqrt{k_B T/ma^2}$ is the angular frequency of a single helix driven by the same torque. Evidently, the force on the helices along their radial distance is approximately zero—we find $\langle F_x \rangle R_h/M \approx 2.3 \times 10^{-5} \pm 8 \times 10^{-6}$—consistent with the findings of ref. 34. However, the tangential forces are large and point in opposite directions. The rotation of a helix creates a flow field, which tries to drag the other helix in a tangential direction. We expect this force to be the main mechanism of helix wrapping and bundle formation. In ref. 34, a "tipping" momentum has been determined, which expresses the same effect.

The magnitude of the tangential force depends on the distance between the helices. As shown in Fig. 3, the force exhibits two power-law regimes. At distances $d/R_h < 5$, $F \sim 1/d$, which is explained by the distance dependence of the flow field generated by a rotating infinitely long cylinder.[62] With increasing distance, the flow field will be modified due to the finite length of the helices. Hence, for $d/R_h > 5$, we observe a crossover of the force corresponding to the flow field created by a spinning sphere, which yields a $F \sim 1/d^2$ dependence for these distances.

3.2 Three helices

3.2.1 Synchronization and bundling dynamics. To study bundle formation, we now consider three helices placed on an
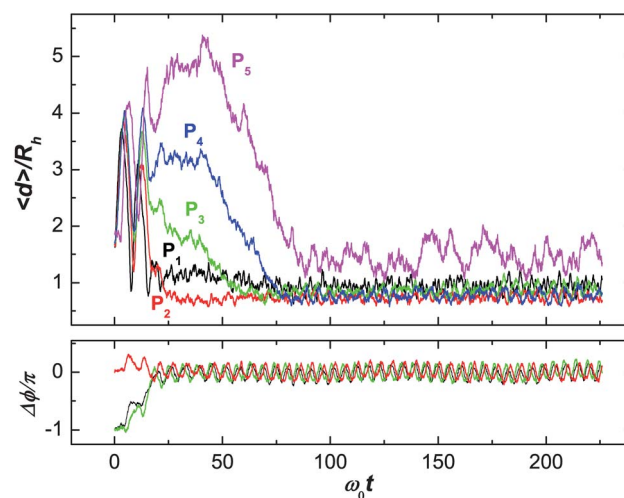

Fig. 4 Phase angle difference and average distances between equivalent points $P_i = iP$ along the helix contour as a function of time for the separation $d/R_h = 2.5$. The three helices have the initial phase differences $\Delta\phi_{12} = -\pi$ (black), $\Delta\phi_{13} = 0$ (red), and $\Delta\phi_{32} = -\pi$ (green).
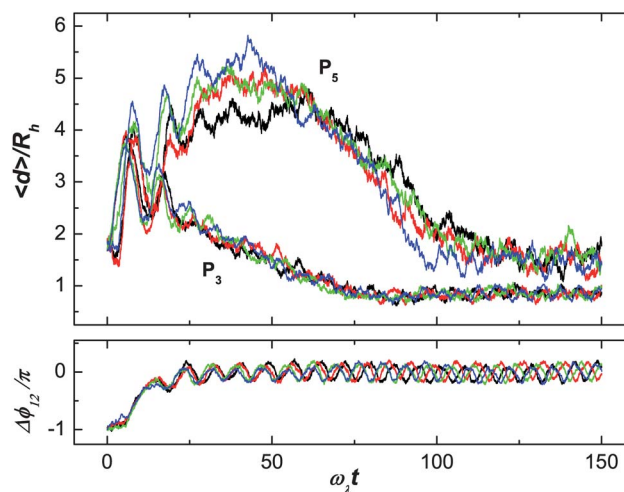
Fig. 5 Phase angle difference $\Delta\phi_{12}$, for the initial value $\Delta\phi_{12} = -\pi$, and average distances between equivalent points at P_3 and P_5 along the helix contour as a function of time for the separation $d/R_h = 2.5$. The various single realization curves are obtained for the MPC time steps $h/\sqrt{ma^2/(k_B T)} = 0.01$ (black), 0.02 (red), 0.05 (green), and 0.1 (blue), with the angular velocities $\omega_\lambda \sqrt{ma^2/(k_B T)} = 0.0153, 0.0302, 0.0732, 0.138$, respectively.

equilateral triangle with the distance $d/R_h = 2.5$ between their central beads. Initially, they are aligned in parallel. There is no axial potential, thereby the tails of the helices are free to bend according to the induced hydrodynamic forces. Initially, two of them are in-phase with each other and the third is out-of-phase with the phase difference π. The phase-angle differences are defined as $\Delta\phi_{ij} = (\phi_i - \phi_j)$ ($i \neq j = 1,2,3$), where the phase angle ϕ_i of helix i is defined by the orientation of the vector between the central bead of its confined part and the first bead of the helix in the base plane. The initial values are $\phi_1 = -\pi$, $\phi_2 = 0$, and $\phi_3 = -\pi$. Each helix is driven by the same torque $M/k_B T = 800$. The phase angle differences and time averaged distances $\langle d \rangle$ between
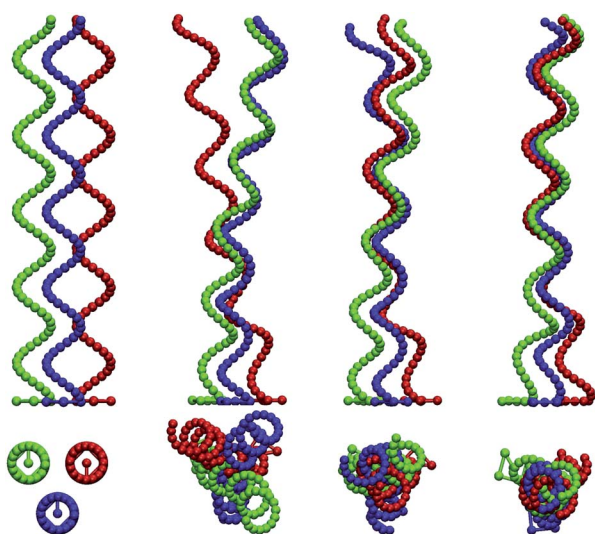
Fig. 6 Snapshots, side views (top) and top views (bottom), of various stages of the bundling process for $d/R_h = 3.5$. From left to right: (i) Initial state, the red helix is out of phase. (ii) The helices synchronized their rotation and start to bundle. (iii) Parts of the helices are bundled. (iv) Final, bundled state. Simulation animations are shown as movie S1 in the ESI†.

the beads of the various helices are shown in Fig. 4 as a function of time at various points P_i along the helices. The equivalent bead positions P_i along a helix contour are $P_i = iP$ ($i = 1$–5), see Fig. 1. After a short time of only about four helix rotations, the phase differences $\Delta\phi_{12}$ and $\Delta\phi_{32}$ converged to zero; $\Delta\phi_{13} \approx 0$, because helices 1 and 3 remain in-phase independent of time. In the steady state, all the phases are synchronized and exhibit an oscillating behavior due to excluded-volume interactions of the bend helices. The frequency is equal to the mean rotational frequency of the bundle. The average distances converge to plateau values after some time, which marks the time necessary for bundle formation. We consider the bundling process to be finished when the distances at the tail have reached their stationary-state value. For tight bundles, the minimum distance between the helices is determined by the bead excluded-volume distance ($d/a \approx 1$). The stationary-state distances are assumed in sequence from P_1 to P_5, which implies that bundling occurs from the anchoring plane to the tail. Note that all phase differences have converged before the average distances for the various P_i assume their stationary-state values. This implies that synchronization occurs before bundle formation.

Our mesoscale simulations are performed at finite Reynolds numbers. With the rotation frequency $\omega_0 = 0.113\sqrt{k_BT/ma^2}$, the helix radius and the solvent kinematic viscosity of Sec. 2.3, the Reynolds number is $Re = \omega_0 R_h^2/\nu \approx 0.5$ for the collision time step $h = 0.1\sqrt{ma^2/(k_BT)}$. Since $Re < 1$, but not much smaller than unity, the question arises of the relevance of non-linear terms in the Navier–Stokes equations. To demonstrate that the observed dynamical behavior corresponds to the low Reynolds-number regime, we show in Fig. 5 phase angle differences and average distances for various collision time steps in the range $h/\sqrt{ma^2/k_B} = 0.01 - 0.1$. Note that the viscosity of the MPC solvent is essentially inversely proportional to h in the considered range.[37,38] Since at fixed torque, the rotation frequency is $\omega_\lambda \sim 1/$

$\nu \sim h$, this corresponds to the range of Reynolds numbers $Re = 6\times10^{-3} - 0.6$ and, hence, covers two orders of magnitude. Evidently, we obtain, within the statistical fluctuations the same time-dependent behavior for every collision step, which supports our conclusion that the results reflect the system behavior at low Reynolds numbers.

Fig. 6 displays snapshots for various stages of the bundling process. Starting from an aligned initial state, tangential hydrodynamic forces (see Sec. 3.1) cause a tilt of the individual helices, which brings them in closer contact near their fixed ends and simultaneously separates their free ends. This is quantitatively reflected in Fig. 4, where the mean distance at P_2 approaches its stationary-state value while P_5 increases initially and is still far from the stationary-state value. Naturally, the details depend on the separation d. In the stationary state a compact bundle is formed, where the helices are wrapped around each other. A similar behavior of attraction after synchronization was observed in other biological systems, such as sperm pairs[55,63] or synthetic swimmers,[64] which are swimming together.

3.2.2 Helix winding. A winding angle Φ_{ij} is calculated between two helices i, j according to

$$\cos(\Phi_{ij}) = \langle \boldsymbol{u}_{ij}^{end}(t)\boldsymbol{u}_{ij}^{end}(0)\rangle, \qquad (11)$$

where $\boldsymbol{u}_{ij}^{end}(t) = (\boldsymbol{R}_i^{end}(t) - \boldsymbol{R}_j^{end}(t))/|\boldsymbol{R}_i^{end}(t) - \boldsymbol{R}_j^{end}(t)|$ and $\boldsymbol{R}_i^{end}$ is the position vector of the tail end of helix i, to quantitatively measure their wrapping. A value of $\Phi_{ij} = 2\pi$ indicates that the helices wrapped once around each other.[35] As displayed in Fig. 7, Φ_{ij} is initially zero and increases as the helices start to bundle. When the torque is small, loose bundles are formed due to weak hydrodynamic interactions. For large torques, tighter bundles appear. In the case of the five turn helices, the winding angle increases from $\Phi_{ij} \approx \pi$ to $\Phi_{ij} \approx 2\pi$ with increasing torque for the considered range of M. Interestingly, we obtain a logarithmic dependence of the stationary state winding angle on the applied momentum, i.e., a rather weak dependence, as shown in the inset of Fig. 7.

We find a similar behavior for the tightness of the bundles, when we vary the initial helix separation. With increasing separation, smaller winding angles are obtained and correspondingly looser bundles. At small separations follow larger winding angles and correspondingly tighter bundles.

In our simulations, the mechanical constraints due to excluded-volume interactions can be turned off in order to unravel their effect on bundle formation. Without such an interaction we still observe bundles, which are tighter for $M/k_BT > 400$, because the helices can strongly overlap in space. Not surprisingly, the winding angle continues to increase without converging to a finite value, but the rotation of the helices is synchronized.

3.2.3 Synchronization and bundling times. After bundle formation is complete, we determine the average distances between the helices and the bundling times for the various $P_i = iP$. Average bead distances for several d are shown in Fig. 8. The helices make a tight bundle for small distances. As the separation increases, the size of the bundled domain decreases. Note that the tail part of the bundle has a larger separation than the middle
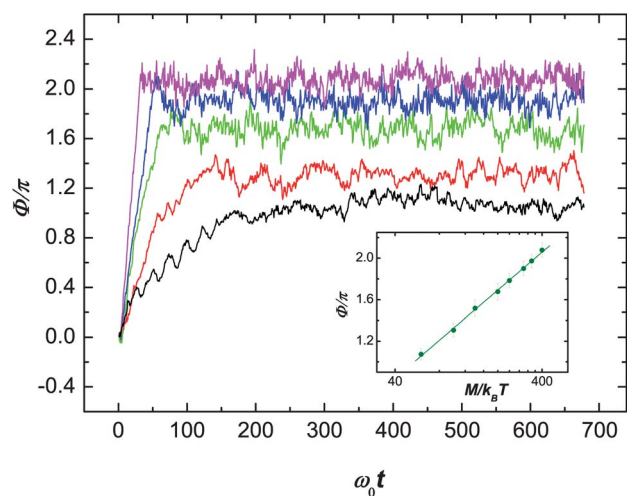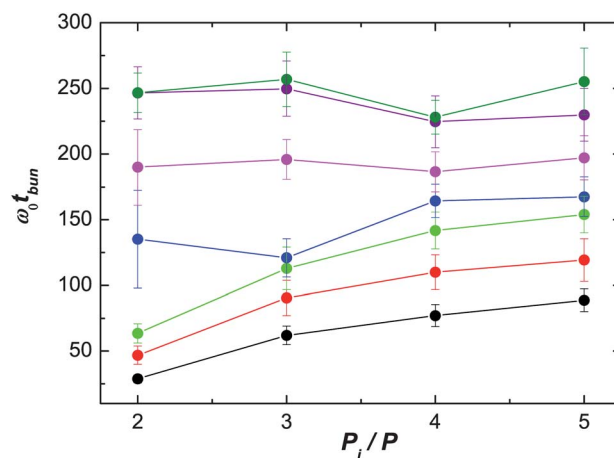
Fig. 7 Winding angle Φ as a function of time for three helices with separation $d/R_h = 2.5$. The lines from the bottom to the top correspond to the torques $M/k_BT = 240, 400, 800, 1200,$ and 1600. Tighter bundles are formed as the torque increases. Inset: Logarithmic dependence of the winding angle on the applied torque.
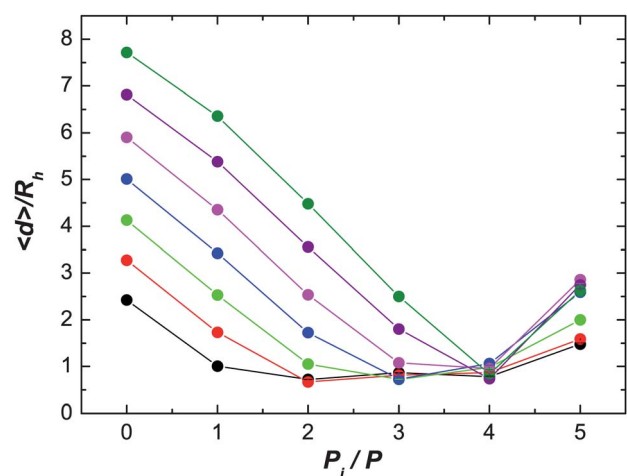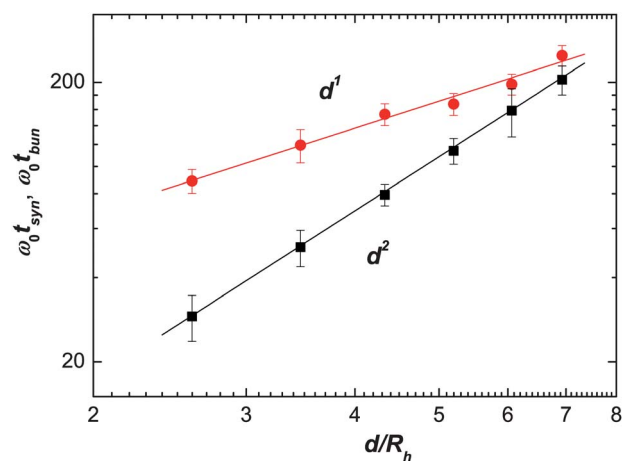

Fig. 8 Average distances between three helices at the various P_i for the initial values $d/R_h = 2.5, 3.5, 4.3, 5, 6, 7, 7.8$ (bottom to top at $P_i = 0$) in the bundled state. The torque is $M/k_BT = 800$.

Fig. 9 Bundling time for a system of three helices as function of P_i. The initial separations are $d/R_h = 2.5, 3.5, 4.3, 5, 6, 7, 7.8$ (bottom to top), and the torque is $M/k_BT = 800$.

Fig. 10 Synchronization (black) and bundling (red) times as a function separation for a system of three helices. The synchronization time increases as $t_{syn} \sim d^2$ and the bundling time as $t_{bun} \sim d$. For large separations, bundling and synchronization occur simultaneously.

part, which is consistent with previous studies.[5,35] The average distance at the tail region is about 1.5–3 times larger than the smallest distance in the tightly bundled middle region. The larger distances at the bundle end are determined by the force balance between the mechanical force, specifically excluded-volume interactions, opposing wrapping, and hydrodynamic interactions promoting bundling. This is supported by simulations where the purely repulsive Lennard–Jones forces are turned off. Here, the ends of the helices come significantly closer. Moreover, when the torque is increased or the initial separation is decreased, the end distances decrease due to an increase of hydrodynamic interactions.

The bundling times t_{bun} are presented in Fig. 9 for several distances d. As explained above, t_{bun} is defined as the time when bundling is finished and the distances between the helices at tail region (P_5) have converged to a steady-state value. Evidently,

bundling for small separations is faster than that for large separations. Moreover, the bundling times for the various P_i increase along the bundle from $i = 2$ to $i = 5$ for $d/R_h \lesssim 5$. For larger d, bundling happens almost simultaneously along the helices, because the helices touch near their free end only (see Fig. 12).

Synchronization and bundling times are presented in Fig. 10 as a function of helix separation. The synchronization time is defined as the time when the phase differences between all helices have converged to stationary oscillating values. Note that synchronization occurs before bundle formation. As d increases, the synchronization and bundling times increase as

$$t_{syn} \sim d^2 \text{ and } t_{bun} \sim d. \tag{12}$$

At large separations, synchronization and bundling occur almost simultaneously.

Based on the numerical results presented in Fig. 4, 7, 9, and 10, we propose the following synchronization and bundling

mechanism. For short distances, direct hydrodynamic interactions start to induce synchronization when the flagella are still oriented in parallel, and is completed when the flagella first come into close contact at P_2 (see Fig. 4). However, the time for synchronization due to direct hydrodynamic interactions quickly increases with increasing distance. This time has been estimated theoretically to increase as d^5, within the hydrodynamic far-field approximation, for a related system of two rigid dumbbells with their midpoints fixed by stiff springs.[12] Furthermore, in our simulations, direct hydrodynamic synchronization is only possible if the helix rotation time $2\pi/\omega_0$ is much longer than the vorticity diffusion time $d^2/(4\pi^2 v)$; for our parameters, this implies that synchronization due to direct hydrodynamic interactions is only possible for $d/R_h \ll 25$. For larger distances, the flagella initially can only feel the average rotational flow field generated by all helices together. Since a single helix generates a rotational flow field with angular component $v_\varphi(r) \sim \omega_0 R_h^2/r$, each flagellum is exposed to a flow of magnitude $\omega_0 R_h^2/d$ in a tangential direction. It follows this flow—by tilting near the anchoring point, where the torque is largest—until the flagellar tail has rotated (about the central line of the whole bundle) by about 180°, so that the flagella come in close contact somewhere along their contour. Near the point of close contact, the hydrodynamic interactions become very strong and lead to rapid synchronization. Thus, we can estimate the synchronization time in this regime as
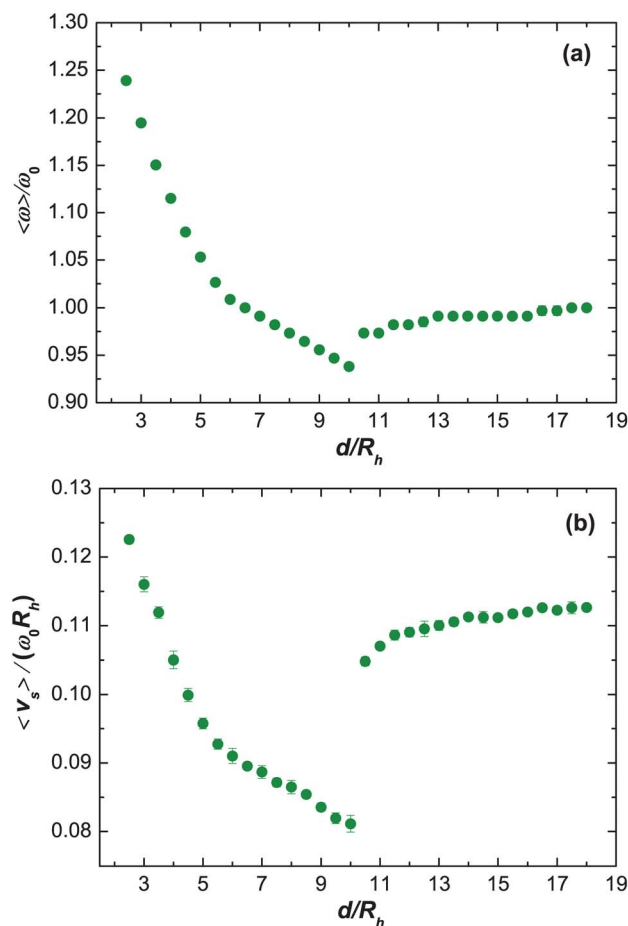
$$\omega_0 t_{syn} \sim \omega_0 \int_0^\pi d\varphi \ d/v_\varphi(d) \sim (d/R_h)^2. \quad (13)$$
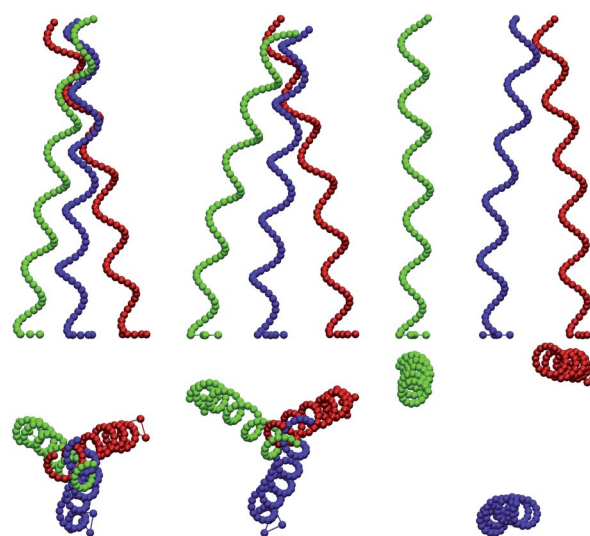
This is consistent with the power law obtained in Fig. 10

After the flagella have synchronized and come into close contact, the tangential forces (Fig. 2) lead to a wrapping, which promotes helix bundling close to the contact point. Then, the "bundling front" propagates towards the free ends (see Fig. 9). Eventually, at very large distances d, synchronization and bundling is prevented by hydrodynamic interactions which are too weak to overcome the bending rigidity or fluid noise which is too strong, and the helices rotate independent of each other.

3.2.4 Rotation frequency and fluid velocity. Fig. 11 (a) shows average angular velocities $\langle \omega \rangle$ in the stationary rotating state. As the separation between the helices increases, the angular velocity decreases for $d/R_h \lesssim 10$. Two linear regimes can be identified, a regime where $\langle \omega \rangle$ drops quickly for small distances $d/R_h < 5$, corresponding to tight bundles, and a regime of a slower

Fig. 12 Snapshots, side views (top) and top views (bottom), of three helices for the separations $d/R_h = 7.5$ (left), 10 (middle), 12.5 (right) in the stationary state. Simulation animations are shown as movie S2 in the ESI†.

Fig. 11 Average bundle angular-velocities of three helices (a) and average fluid velocities (b) as a function of separation. At separations $d/R_h > 10$, the helices behave like individual ones.
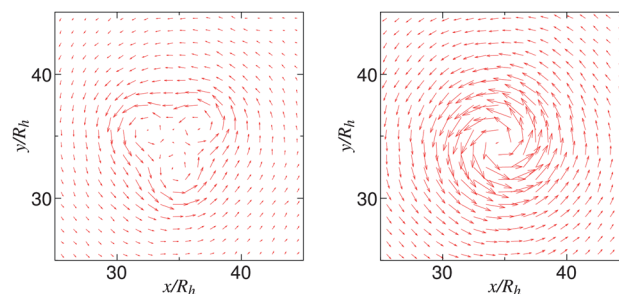
Fig. 13 Fluid streamlines around a bundle of three helices at the region of their fixed ends (P_0, left) and the middle region (P_2, right).

variation for larger distances $5 < d/R_h < 10$, corresponding to loose bundles. For $d/R_h > 10$, the helices rotate independently with a frequency close to that of a single helix. The snapshots of Fig. 12 illustrate stationary-state conformations for various separations (see also Fig. 6). In response to helix rotation, the fluid moves along the z-direction. The average fluid velocities $\langle v_s \rangle = \sum_{i=1}^{N_S} \langle v_i \rangle / N_S$ displayed in Fig. 11 (b) show a similar dependence on separation d as the angular velocity $\langle \omega \rangle$. Only the discontinuity is larger at the crossover distance from bundled to free helices. The minimum at $d/R_h \approx 10$ indicates that loosely, end-bundled helices exhibit a somewhat smaller rotation frequency and fluid velocity than those rotating independently ($d/R_h > 10$). The reduced swimming velocity in the regime $5 < d/R_h < 10$ is due to the tilt of the flagella with respect to each other (see Fig. 12), which reduces thrust in the swimming direction. Hence, we conclude that bacteria with large bundled domains gain swimming velocity by the larger rotational velocity, while bacteria with only small bundled domains loose swimming velocity. Bundles with large domains exhibit an approximately 20% higher rotation frequency than individual helices. A similar small difference between a single-filament rotation frequency and a bundle rotation rate has been found experimentally. [14] Therefore, flagella with only partially bundled domains possess no benefit of larger swimming velocities over separated, individual helices.

The fluid streamlines, generated by the rotating bundle for $d/R_h = 2.5$ are shown in Fig. 13. The bundled helices rotate counterclockwise producing a counterclockwise rotating fluid. In Fig. 13 (left), three helices are visible, whereas in the middle part of the bundle only streamlines of a single unit are visible.

3.3 Several helices

In bacteria such as *E. coli* or *Salmonella typhimurium*, typically half a dozen flagella are included in a bundle.[65] To unravel differences and similarities of bundles composed of several flagella, we compare the bundling behavior of systems from three up to six helices. Fig. 14 displays snapshots of conformations during the bundling process of six helices. The helix centers are placed on a regular triangle, square, pentagon, and hexagon, respectively, with a circumscribed circle of radius r in the xy-plane. In all cases, the average distances between the individual beads and the winding angles between helices show a similar behavior as in the three helices case (*cf.* Fig. 7, 8), that is a tighter bundle is formed with increasing torque.

Results for bundling times are presented in Fig. 15 for $N_h = 3$, 4, 5, 6 helices and various radii r. By varying the applied torque, the bundling time decreases with increasing torque according to $t_{bun} \sim M^{-1}$ (see Fig. 15 (a)). The bundling times for the torque $M/k_B T = 800$, displayed in Fig. 15 (b), indicate that the bundling time increases as $t_{bun} \sim r$ with the radius. Both, figures reveal that t_{bun} decreases with increasing number of helices. This is quantitatively shown in Fig. 15 (c) for various radii r. Typically, the bundling time decays as $t_{bun} \sim N_h^{-1/2}$. Hence, we find that the bundling time follows the scaling law

$$t_{bun} \sim r N_h^{-1/2} M^{-1}. \tag{14}$$
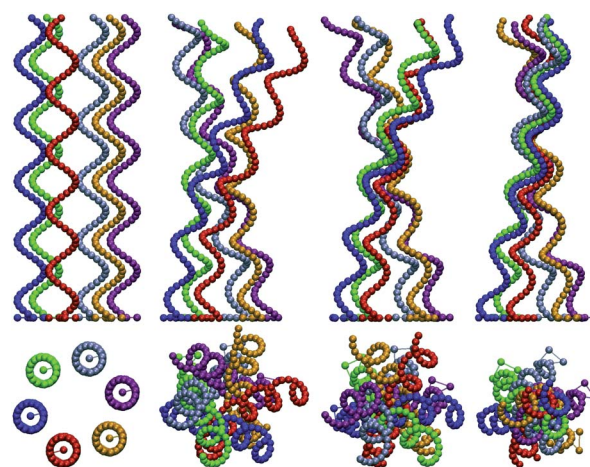
Fig. 14 Snapshots, side views (top) and top views (bottom), of various stages of the bundling process for $r/R_h = 3.5$. Left to right: (i) Initial state, the red helix is out of phase. (ii) The helices synchronized their rotation. (iii) The helices start to bundle. (iv) Final, bundled state. Simulation animations are shown as movie S3 in the ESI†.

The r dependence is consistent with the dependence on d obtained for three flagella in Sec. 3.2, since for any given number N_h, $d = 2r\sin(\pi/N_h)$. Then, for the range $2 < N_h < 7$, the increase in bundling time can be approximated by the effective power-law $N_h^{1/3}$ at a given distance d. We can express t_{bun} by $t_{bun} \sim \rho^{-1/2} M^{-1}$, where $\rho = N_h/(2\pi r^2)$ is the planer density of helices. Our results indicate that either an increasing helix density or an increasing torque enhances the efficiency of the bundle formation which we attribute to the more pronounced hydrodynamic interactions. Furthermore, bundle formation can be controlled more easily by adopting the applied torque than changing the density of helices.
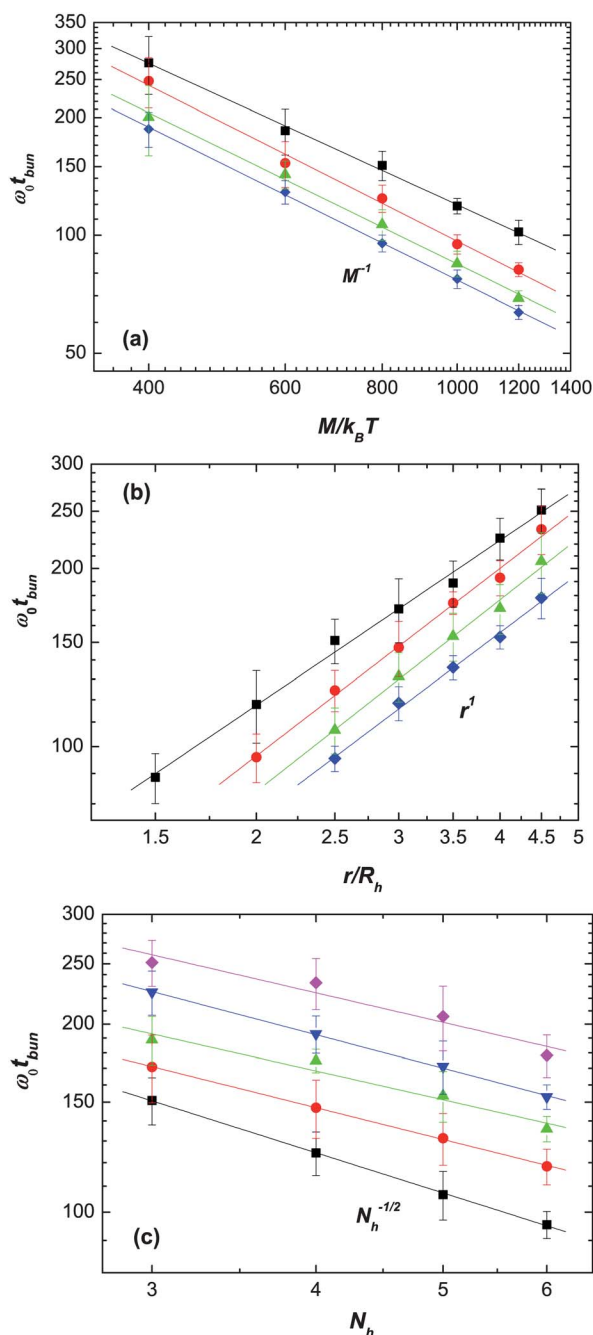
4 Summary and conclusions

The synchronization and bundling behavior of several bacterial flagella has been investigated by the multiparticle collision dynamics approach. A flagellum has been described by a bead-spring model with internal potentials to account for the helical structure.

To reveal the forces determining bundle formation, a system of two parallel aligned helices has been considered. Calculating the force on each helix, we find that the dominant contributions are tangential to the distance vector between the helices and point in opposite direction. The force itself is due to hydrodynamic interactions between the helices, and decays by two power-law regimes with increasing helix distance. We would like to point out that our helices are flexible and the confining potentials allow for fluctuations. This is important, since rigid helices have been shown to exhibit no synchronization.[11,34]

A prerequisite of helix bundling is synchronization of their rotational motion.[3,4] Considering a system of three five-turn helices driven by the same torque, where one of them is initially out of phase by a phase angle π, we find fast synchronization with a synchronization time which increases as $t_{syn} \sim d^2$ with increasing separation. The subsequent bundling process starts close to the fixed ends of the flagella for small separations, *i.e.*,

In the stationary state, our systems are force free along the z-direction, *i.e.*, the swimming direction, and the fluid moves with a constant average velocity in the positive z-direction (see Fig. 11). Hence, the helices pump fluid in response to their rotation. As shown in Fig. 11, tighter bundles with large bundled domains marginally enhance the swimming efficiency over loose bundles with partially bundled domains, as is reflected by the larger fluid velocity for $d/R_h < 4$ compared to that of individual helices. Loosely bundled flagella display no benefit in swimming velocity compared to an individual helix. This explains why bacteria with multiple flagella do not swim faster than those with a single flagellum.[14,66] Thus, from a evolutionary point of view, the benefit of multiple flagella compared to a single flagellum is to allow "run and tumble" motion, rather than swimming efficiency.[66]

Extending our studies to systems of up to six helices, we find that the bundling time follows the dependence $t_{\text{bun}} \sim \rho^{-1/2} M^{-1}$, which indicates that bundle formation is more sensitive to the applied torque than the density of helices. This is related to the strength of hydrodynamic interactions, the driving force of bundle formation. Large torques imply strong flows and hydrodynamics dominate over fluid fluctuations. Similarly, an increasing number density leads to stronger inter-helix interactions.

In the present study, one of the ends of the helices is fixed in space and each experiences a net torque. In swimming bacteria, the net torque on the whole bacterium is zero. Hence, the overall flow field is different from that presented in Fig. 13, because the counter-rotating head of the bacterium creates an oppositely rotating field.[15] Nevertheless, the flow profile in the tail region will be similar to that of Fig. 13. The additional rotation of the bacterium body enhances bundle formation and could be an important factor, outweighing hydrodynamic interactions.[9] Simulation studies with swimming bacteria are under-way, which will provide detailed insight into the interplay between flagella and body rotation in bundle formation.

Acknowledgements

References

1 H. C. Berg and R. A. Anderson, *Nature*, 1973, **245**, 380–382.
2 H. C. Berg, *E. coli in Motion*, Springer, New York, 2004.
3 R. M. Macnab, *Proc. Natl. Acad. Sci. U. S. A.*, 1977, **74**, 221–225.
4 M. Kim, J. C. Bird, A. J. V. Parys, K. S. Breuer and T. R. Powers, *Proc. Natl. Acad. Sci. U. S. A.*, 2003, **100**, 15481–15485.
5 H. Flores, E. Lobaton, S. Mendez-Diez, S. Tlupova and R. Cortez, *Bull. Math. Biol.*, 2005, **67**, 137–168.
6 J. J. L. Higdon, *J. Fluid Mech.*, 1979, **94**, 331–351.
7 J. J. L. Higdon, *J. Fluid Mech.*, 1979, **90**, 685–711.
8 E. M. Purcell, *Proc. Natl. Acad. Sci. U. S. A.*, 1997, **94**, 11307–11311.
9 T. R. Powers, *Phys. Rev. E: Stat. Phys., Plasmas, Fluids, Relat. Interdiscip. Top.*, 2002, **65**, 040903.
10 Y. Gebremichael, G. S. Ayton and G. A. Voth, *Biophys. J.*, 2006, **91**, 3640–3652.

Fig. 15 Bundling time as a function of the applied torque (a), radius r (b), and helix number (c). (a) The radius is $r/R_h = 2.5$, and the number of helices $N_h = 3$ (black), 4 (red), 5 (green), 6 (blue). (b) The torque is $M/k_B T = 800$; the helix numbers are the same as in (a). (c) The radii are $r/R_h = 2.5$ (black), 3 (red), 3.5 (green), 4 (blue), 4.5 (purple), and the other parameters are the same as in (a), (b). The lines are obtained by linear regression.

tight bundles, and proceeds toward the tail end. At larger separations and loose bundles, only the tail-end parts meet (see Fig. 12). In any case, the time until bundling is finished depends linearly on distance $t_{\text{bun}} \sim d$, where $t_{\text{syn}} < t_{\text{bun}}$. By calculating a winding angle,[35] we find tighter bundles at larger torques. Moreover, the winding angle shows that left-handed helices twist around each other in a right-handed manner without jamming.[3,4]

11 M. Reichert and H. Stark, *Eur. Phys. J. E*, 2005, **17**, 493–500.
12 B. Qian, D. A. Gagnon, K. S. Breuer and T. R. Powers, *Phys. Rev. E: Stat., Nonlinear, Soft Matter Phys.*, 2009, **80**, 061919.
13 L. Turner, W. S. Ryu and H. C. Berg, *J. Bacteriol.*, 2000, **182**, 2793–2801.
14 N. C. Darnton, L. Turner, S. Rojevsky and H. C. Berg, *J. Bacteriol.*, 2007, **189**, 1756–1764.
15 N. Watari and R. G. Larson, *Biophys. J.*, 2010, **98**, 12–17.
16 H. C. Berg and D. A. Brown, *Nature*, 1972, **239**, 500–504.
17 D. Coombs, G. Huber, J. O. Kessler and R. E. Goldstein, *Phys. Rev. Lett.*, 2002, **89**, 118102.
18 H. Hotani, *J. Mol. Biol.*, 1982, **156**, 791–806.
19 C. R. Calladine, *Nature*, 1975, **225**, 121–124.
20 C. R. Calladine, *J. Mol. Biol.*, 1978, **118**, 457–479.
21 N. C. Darnton and H. C. Berg, *Biophys. J.*, 2007, **92**, 2230–2236.
22 H. Wada and R. R. Netz, *Europhys. Lett.*, 2008, **82**, 28001.
23 R. E. Goldstein, A. Goriely, G. Humber and C. W. Wolgemuth, *Phys. Rev. Lett.*, 2000, **84**, 1631–1634.
24 J. W. Shaevitz, J. Y. Lee and D. A. Fletcher, *Cell*, 2005, **122**, 941–945.
25 H. Wada and R. R. Netz, *Phys. Rev. Lett.*, 2007, **99**, 108102.
26 H. Wada and R. R. Netz, *Phys. Rev. E: Stat., Nonlinear, Soft Matter Phys.*, 2009, **80**, 021921.
27 R. Vogel and H. Stark, *Eur. Phys. J. E*, 2010, **259**, 33.
28 R. M. Macnab and M. K. Ornston, *J. Mol. Biol.*, 1977, **112**, 1–30.
29 G. I. Taylor, *Proc. R. Soc. London, Ser. A*, 1951, **209**, 447–461.
30 C. R. Calladine, *J. Theor. Biol.*, 1976, **57**, 469–489.
31 J. Lighthill, *SIAM Rev.*, 1976, **18**, 161–230.
32 J. Lighthill, *J. Eng. Math.*, 1996, **30**, 35–78.
33 H. C. Berg, *Annu. Rev. Biochem.*, 2003, **72**, 19–54.
34 N. Kim and T. R. Powers, *Phys. Rev. E: Stat., Nonlinear, Soft Matter Phys.*, 2004, **69**, 061910.
35 P. J. A. Janssen and M. D. Graham, *Phys. Rev. E: Stat., Nonlinear, Soft Matter Phys.*, 2011, **84**, 011910.
36 R. Kapral, *Adv. Chem. Phys.*, 2008, **140**, 89–146.
37 G. Gompper, T. Ihle, D. M. Kroll and R. G. Winkler, *Adv. Polym. Sci.*, 2009, **221**, 1–87.
38 M. Ripoll, K. Mussawisade, R. G. Winkler and G. Gompper, *Phys. Rev. E: Stat., Nonlinear, Soft Matter Phys.*, 2005, **72**, 016701.
39 J. T. Padding and A. A. Louis, *Phys. Rev. Lett.*, 2004, **93**, 220601.
40 M. Hecht, J. Harting, T. Ihle and H. J. Herrmann, *Phys. Rev. E: Stat., Nonlinear, Soft Matter Phys.*, 2005, **72**, 011408.
41 K. Tucci and R. Kapral, *J. Phys. Chem. B*, 2005, **109**, 21300.
42 S. H. Lee and R. Kapral, *J. Chem. Phys.*, 2005, **122**, 214916.
43 J. T. Padding and A. A. Louis, *Phys. Rev. E: Stat., Nonlinear, Soft Matter Phys.*, 2006, **74**, 031402.
44 A. Wysocki, C. P. Royall, R. G. Winkler, G. Gompper, T. H, A. van Blaaderene and H. Löwen, *Soft Matter*, 2009, **5**, 1340.
45 T. Franosch, M. Grimm, M. Belushkin, F. M. Mor, G. Foffi, L. Forró and S. Jeney, *Nature*, 2011, **478**, 85.
46 A. Malevanets and J. M. Yeomans, *Europhys. Lett.*, 2000, **52**, 231–237.
47 K. Mussawisade, M. Ripoll, R. G. Winkler and G. Gompper, *J. Chem. Phys.*, 2005, **123**, 144905.
48 S. H. Lee and R. Kapral, *J. Chem. Phys.*, 2006, **124**, 214901.
49 J. F. Ryder and J. M. Yeomans, *J. Chem. Phys.*, 2006, **125**, 194906.
50 I. Ali, D. Marenduzzo and J. M. Yeomans, *Phys. Rev. Lett.*, 2006, **96**, 208102.
51 R. Chelakkot, R. G. Winkler and G. Gompper, *Europhys. Lett.*, 2010, **91**, 14001.
52 C.-C. Huang, R. G. Winkler, G. Sutmann and G. Gompper, *Macromolecules*, 2010, **43**, 10107–10116.
53 L. McWhirter, H. Noguchi and G. Gompper, *Proc. Natl. Acad. Sci. U. S. A.*, 2009, **106**, 6039–6043.
54 H. Noguchi and G. Gompper, *Proc. Natl. Acad. Sci. U. S. A.*, 2005, **102**, 14159–14164.
55 Y. Yang, J. Elgeti and G. Gompper, *Phys. Rev. E: Stat., Nonlinear, Soft Matter Phys.*, 2008, **78**, 061903.
56 J. Elgeti, U. B. Kaupp and G. Gompper, *Biophys. J.*, 2010, **99**, 1018–1026.
57 G. Rückner and R. Kapral, *Phys. Rev. Lett.*, 2007, **98**, 150603.
58 A. Malevanets and R. Kapral, *J. Chem. Phys.*, 1999, **110**, 8605.
59 C.-C. Huang, A. Chatterji, G. Sutmann, G. Gompper and R. G. Winkler, *J. Comput. Phys.*, 2010, **229**, 168–177.
60 T. Ihle and D. M. Kroll, *Phys. Rev. E: Stat. Phys., Plasmas,Fluids, Relat. Interdiscip. Top.*, 2001, **63**, 02020.
61 M. P. Allen, *Computer Simulation in Liquids*, Oxford, Clarendon, 1987.
62 D. J. Tritton, *Physical Fluid Dynamics*, Clarendon, Oxford, 1988.
63 G. J. Elfring and E. Lauga, *Phys. Rev. Lett.*, 2009, **103**, 088101.
64 C. M. Pooley, G. P. Alexander and J. M. Yeomans, *Phys. Rev. Lett.*, 2007, **99**, 228103.
65 C. Brenner and H. Winet, *Ann. Rev. Fluid. Mech.*, 1977, **9**, 39.
66 R. M. Macnab, *J. Clin. Microbiol.*, 1976, **4**, 258.